Realization of a Multi-Output Quantum Pulse Gate for Decoding High-Dimensional Temporal Modes of Single-Photon States

Laura Serino[*], Jano Gil-Lopez, Michael Stefszky, Raimund Ricken, Christof Eigner, Benjamin Brecht, and Christine Silberhorn

Paderborn University, Integrated Quantum Optics, Institute for Photonic Quantum Systems (PhoQS), Warburgerstraße 100, 33098 Paderborn, Germany

Temporal modes (TMs) of photons provide an appealing high-dimensional encoding basis for quantum information. While techniques to generate TM states have been established, high-dimensional decoding of single-photon TMs remains an open challenge. In this work, we experimentally demonstrate demultiplexing of five-dimensional TMs of single photons with an average fidelity of 0.96 ± 0.01, characterized via measurement tomography. This is achieved with use of a newly developed device, the multi-output quantum pulse gate (MQPG). We demonstrate a proof-of-principle complete decoder based on the MQPG that operates on any basis from a set of six five-dimensional mutually unbiased bases and is therefore suitable as a receiver for high-dimensional quantum key distribution. Furthermore, we confirm the high-quality operation of the MQPG by performing resource-efficient state tomography with an average fidelity of 0.98 ± 0.02.

I. INTRODUCTION

As increasingly more applications for quantum technologies continue to be found, the need to develop a device that enables highly efficient quantum communication (QC) becomes critical [1–3]. Photons are ideally suited for this task due to transmission at the speed of light, intrinsically low decoherence, and their high-dimensional spatial and time-frequency degrees of freedom. These degrees of freedom provide high-dimensional alphabets that allow one to encode more information per photon, leading to important advantages for QC applications, including the higher level of security and efficiency provided by high-dimensional quantum key distribution (HDQKD) with respect to its binary counterpart [4].

Arguably, the most explored high-dimensional photonic degree of freedom is the spatial one, with particular focus on the orbital angular momentum of light. One of the main advantages of this encoding alphabet is the possibility to generate and detect states using time-invariant operations [5–7]. However, this advantage comes with an important drawback, as orbital angular momentum states are inherently incompatible with existing fiber-optic networks and easily degrade in free-space transmission [8].

The time-frequency degree of freedom of photons overcomes this limitation. The standard alphabet based on this degree of freedom is given by time and frequency bins, which can be conveniently generated from an integrated source [9,10]. The manipulation of time-frequency bins and their superpositions is possible with interferometric systems [11] or with a combination of phase modulators and pulse shapers [12,13]. Scaling either of those approaches comes with important challenges, and experimental efforts have been limited to low-dimensional systems [14,15].

To avoid this impediment, we can exploit the time-frequency degree of freedom of light through temporal modes (TMs), i.e., field-orthogonal wave-packet modes. Since TMs span an infinite-dimensional Hilbert space, they can represent any arbitrary time-frequency state of single photons; of particular importance is that they form a natural basis to describe photons generated through ultrafast parametric down-conversion. TMs are characterized by robustness against fiber dispersion and a higher packing density with respect to frequency bins, as they can exploit the full frequency space without the need for guard bands [16,17]. These properties render TMs a valuable resource not only for QC protocols but also for several other applications, from quantum enhanced spectroscopy and metrology [18–20] to quantum memories [21–23] and deterministic photonic quantum gates [24–26].

*laura.serino@upb.de

To fully reap the benefits of high-dimensional encoding, a TM-based QC scheme requires the generation, manipulation, and simultaneous detection of multiple TMs of single photons. Single-photon operation is a requirement as quantum light is used in a wide variety of interfacing and communication protocols. Generation of single photons with a well-defined TM state has been successfully achieved through ultrafast parametric down-conversion [27–29]. Manipulation and detection of single-photon TMs, on the other hand, have been limited to a single TM at a time. These demonstrations were obtained with use of a quantum pulse gate (QPG) [30–32], a TM-selective device based on integrated sum-frequency generation that by design is limited to single-output operation.

In this work, we demonstrate high-dimensional single-photon TM decoding using a multi-output QPG (MQPG). The MQPG is a newly developed device that uses a custom poling structure to project a single-photon-level input signal onto all the elements of a chosen high-dimensional TM alphabet (or their superpositions) and map the results of the projections onto different output frequencies. We then use a single-photon spectrograph to read out the output frequency for each input photon, hence providing the projection result as a "click" in the corresponding output channel. We demonstrate that our device is compatible with single-photon-level input states from a five-dimensional Hilbert space, and characterize its performance by quantum measurement tomography. Thus we showcase a proof-of-principle complete HDQKD decoder based on the MQPG that can work with any basis from a set of six five-dimensional mutually unbiased bases (MUBs). To further confirm the capabilities of our device, we use the reconstructed positive-operator-valued measure (POVM) from the measurement tomography to facilitate a resource-efficient state tomography with an average fidelity of 0.98 ± 0.02. Furthermore, we describe the necessary improvements to scale the decoder scheme to perform high-quality measurements in even higher dimensions.

We note that although preliminary work toward expanding frequency conversion to multi-output operation has been demonstrated [33,34], these implementations were inherently incompatible with single-photon-level input states. Our device allows one to fully exploit the greater information capacity provided by high-dimensional encoding in single photons, granting faster transmission of information and enabling HDQKD protocols [4]. Moreover, the MQPG substantially reduces measurement times for applications that require projections onto a large number of TMs, such as quantum state tomography [31].

II. DEVICE AND PROCESS ENGINEERING

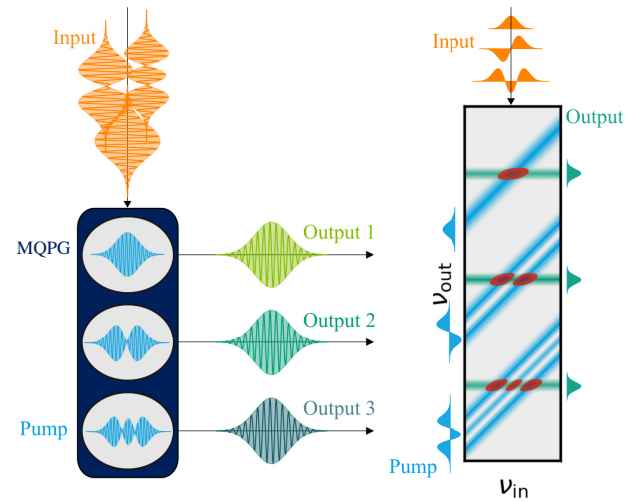A high-dimensional decoder must allow the user to perform a simultaneous high-quality projection of the

FIG. 1. The working principle of the MQPG (left) and description in frequency space (right): in the MQPG waveguide, the input photons (orange) are demultiplexed to different output frequencies (green) on the basis of their TM. The TMs to be measured are selected by shaping the pump field (blue).

input state onto all the elements of a user-chosen basis (Fig. 1). The MQPG achieves this goal through type-II sum-frequency generation (SFG) in periodically poled titanium-in-diffused lithium niobate waveguides. Its operation in frequency space is described by a transfer function G, which maps the input frequencies ν_{in} onto the sum frequencies ν_{out}.

To better understand the nature of the MQPG process, we first describe the simpler single-output process of the QPG [30]. The QPG is a device that selectively up-converts a specific TM component from an input state with an efficiency of up to 87.7%. Such a high conversion efficiency is, in principle, also achievable by the MQPG process.

The transfer function G_0 of the QPG is the product of the pump function α_0, which describes energy conservation, and the phase-matching function Φ_0:

$$G_0(\nu_{\text{in}}, \nu_{\text{out}}) = \alpha_0(\nu_{\text{in}}, \nu_{\text{out}})\Phi_0(\nu_{\text{in}}, \nu_{\text{out}}). \quad (1)$$

The SFG process of the QPG (and the MQPG alike) is dispersion-engineered for group-velocity matching of the pump and input fields, which causes the phase-matching function to be independent of the input frequency [$\Phi_0 \simeq \Phi_0(\nu_{\text{out}})$]. Under the condition that the input and pump bandwidths are significantly broader than the phase-matching bandwidth, the transfer function G_0 becomes separable into a pair of input and output functions [35], meaning that the QPG can perform selective up-conversion of a specific TM. As a consequence, the intensity of the SFG light is proportional to the overlap between the complex spectral amplitudes of the input and pump pulses,
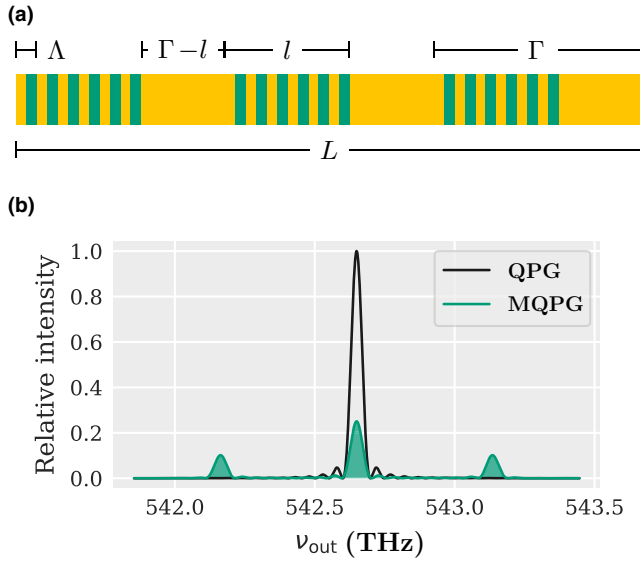
(a)

(b)

FIG. 2. (a) The superpoling pattern of an MQPG waveguide: regions of length l poled with period Λ are alternating with unpoled regions of length $\Gamma - l$, where Γ is the period of this alternation. The regions corresponding to the standard nonlinearity coefficient of the waveguide are shown in yellow, whereas those corresponding to the reversed nonlinearity coefficient are represented in green. (b) A simulation of the phase-matching intensity spectrum of a MQPG (green) compared with that of a QPG (black). The lower efficiency of a MQPG can be compensated with use of higher pump powers.

but does not depend on their relative phase. The latter influences only the overall phase of the SFG light, which is lost in the phase-insensitive photon-counting detection. The pump pulses can be tailored through spectral shaping, allowing one to select the desired TM, transmitting the orthogonal TM components unperturbed.

The inherent limitation of the QPG to a single output channel limits the detection to a single TM at a time, making this device unsuitable for HDQKD, which requires the detection of any element of the chosen basis at every single shot of the communication. In contrast, the multichannel nature of the MQPG renders it suitable for high-dimensional demultiplexing of many TMs into distinct output channels. Each channel j of the MQPG acts as a distinct QPG with its own transfer function G_j and maps a specific TM into the corresponding output frequency. The multipeak phase-matching function $\Phi = \sum_j \Phi_j$ of the MQPG is generated through the alternation of periodically poled and unpoled regions along the waveguide (Fig. 2). The design framework of the MQPG, illustrated in detail in Appendix A, allows one to freely select the spectral parameters such as the interpeak distance and effective number of peaks. One can then shape a pump spectrum $\alpha = \sum_j \alpha_j$ with as many peaks as Φ in order to create a multi-output transfer function such as the one illustrated in Fig. 3.
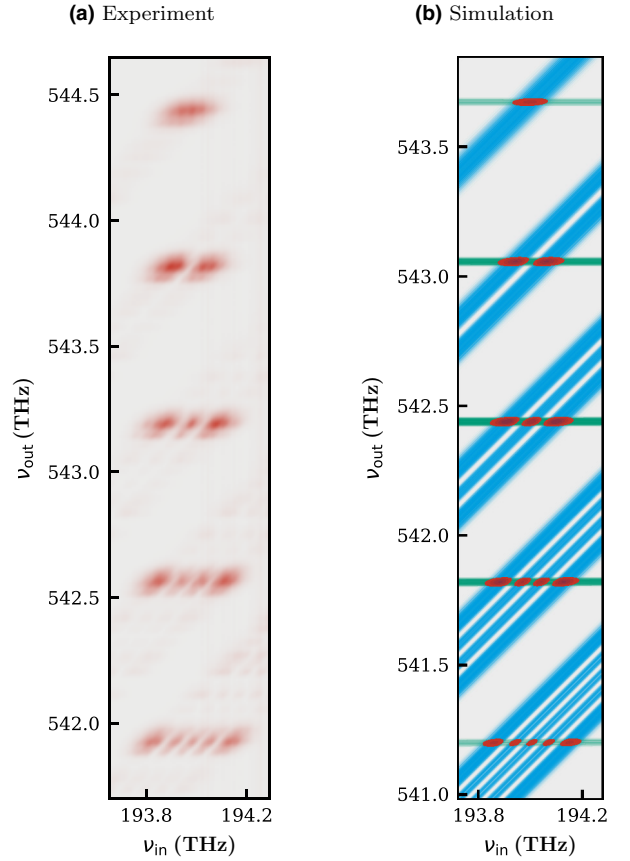
(a) Experiment **(b)** Simulation

FIG. 3. The experimental (a) and simulated (b) transfer function $G(\nu_{\text{in}}, \nu_{\text{out}})$ (red) given by the product of a five-peak phase-matching function $\Phi(\nu_{\text{in}}, \nu_{\text{out}}) \simeq \Phi(\nu_{\text{out}})$ (green) and a five-peak shaped pump spectrum $\alpha(\nu_{\text{in}}, \nu_{\text{out}})$ (blue). The pump peaks are shaped as the first five Hermite-Gaussian modes, and only the intensity of the named quantities is represented. The experimental transfer function resembles well the simulation. On closer inspection, however, it displays a small amount of distortion below the main peaks, which can be attributed to fabrication defects [36]. These imperfections can be removed by applying spectral filtering to each output channel.

For this demonstration, we use a five-peak MQPG waveguide and generate a five-output transfer function to facilitate operation in a five-dimensional space. The experimental transfer function, shown in Fig. 3(a), matches its simulated counterpart [red region in Fig. 3(b)]. The technical specifications of the MQPG waveguide used in this experiment are explained in detail in Appendix A.

III. TOMOGRAPHY THEORY

To quantify the quality of the high-dimensional decoding of the MQPG, we perform quantum measurement tomography [37]. For this purpose, we first introduce the mathematical description of the MQPG operation. We can describe the multi-output decoding as a POVM $\{\pi^\gamma\}$, which corresponds to the complete measurement

basis comprising all the channels of the MQPG. Each individual channel of the MQPG projects the input state onto a user-chosen TM, γ. Consequently, each channel corresponds to a POVM element, i.e., measurement operator, $\pi^\gamma = \sum_{ij} m_{ij}^\gamma |i\rangle\langle j|$ (ideally $|\gamma\rangle\langle\gamma|$), with i and j elements of the fundamental TM basis. We choose to work in a d-dimensional Hilbert space, where d matches the number of channels of the decoder. We select the decoder TMs $\{\gamma\}$ to form a basis for the aforementioned space.

For each MQPG channel, the probability of SFG conversion of a pure input state $\rho^\xi = |\xi\rangle\langle\xi|$ is given by [38]

$$p^{\gamma\xi} = \text{Tr}(\rho^\xi \pi^\gamma). \tag{2}$$

The aim of measurement tomography is to probe the decoder with a full set of input states ρ^ξ so as to reconstruct the full POVM $\{\pi^\gamma\}$. In this work, we use a set of probe states containing all the elements of the $d + 1$ MUBs of our d-dimensional Hilbert space, demonstrating the compatibility of the MQPG with quantum communication protocols based on MUBs, including HDQKD.

IV. EXPERIMENT

A schematic of the experimental setup is shown in Fig. 4. We start from ultrashort Ti:sapphire laser pulses with a spectrum centered at $\lambda_{p,0} = 860$ nm (349 THz) and a repetition rate of 80 MHz. A portion of the beam is directed to a homebuilt 4-f line based on a spatial light modulator [39] with resolution $\delta\nu_{\text{shaper},p} = 10$ GHz to shape the amplitude and phase of its complex spectrum so as to prepare the pump states. The pulse is carved into five peaks with centers separated by $\Delta\nu_{\text{sep}} = 0.63$ THz, each shaped as an element of a five-dimensional TM basis. For this experiment, we choose Hermite-Gaussian (HG) modes and their superpositions, as they provide a good approximation of the natural modes of parametric down-conversion processes [40]. The remaining part of the pulse train pumps an optical parametric oscillator that generates pulses centered at $\lambda_{\text{in},0} = 1545$ nm (194 THz). The beam is attenuated to the single photon level with a mean photon number per pulse lower than 0.1 (0.097 ± 0.001 photons per pulse) and is shaped with use of a commercial wave-shaper with resolution $\delta\nu_{\text{shaper,in}} = 1$ GHz to prepare the input state. The shaping parameters for the input beam and each pump peak are chosen such that the FWHM of the fundamental HG mode is $\Delta\nu_p = \Delta\nu_{\text{in}} = 0.14$ THz. Both beams are then coupled into the MQPG waveguide, each with a coupling efficiency of approximately 60%. The waveguide is designed to be spatially single mode for telecommunication light, and particular care is taken to ensure the pump field is coupled in the fundamental spatial mode.

The multi-output SFG process of the MQPG generates output fields at multiple frequencies (each defining an output channel) around 552 nm (543 THz) based on the TM
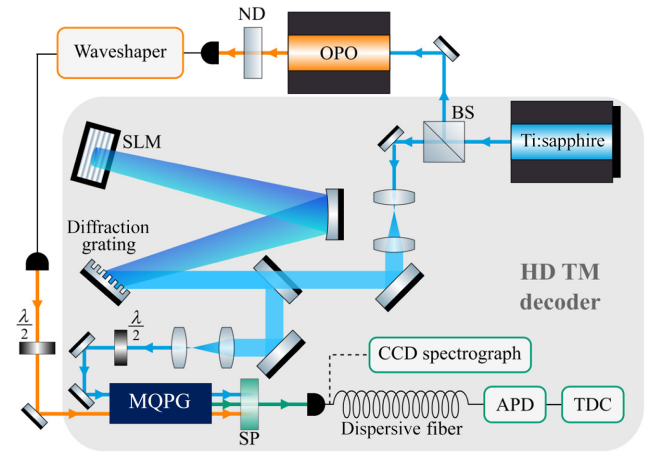

FIG. 4. The experimental setup. A portion of the pump beam (blue line) generated by the Ti:sapphire laser is directed to a 4-f line based on a spatial light modulator (SLM). The shaped beam travels back through the folded configuration at a lower angle than the incoming beam, so as to be picked up by a short mirror and to be coupled into the MQPG waveguide. The remaining part of the Ti:sapphire beam pumps an optical parametric oscillator (OPO) that generates the input beam (orange line) of the experiment at telecommunication wavelengths. The input beam is attenuated to the single-photon level by neutral-density filters (ND) and is shaped with use of a commercial waveshaper, before being coupled into the MQPG waveguide. The output field (green line), isolated by a short-pass filter (SP), is detected either with a commercial CCD spectrograph or with a TOF spectrograph consisting of a dispersive fiber, an avalanche photodiode (APD), and a time-to-digital converter (TDC). The gray area indicates the components of our high-dimensional (HD) TM decoder (for more information, see the main text).

state of the input field. Effectively, the MQPG projects the input TM onto the chosen TM basis and maps the results to the corresponding output frequencies. The internal conversion efficiency is approximately 5%, here limited by the pump pulse energy available in this experiment. The output fields are separated from the residual pump and input fields with use of a dichroic mirror and are then fiber-coupled and measured with a commercial CCD spectrograph (Andor Shamrock 500i) with a resolution of 30 GHz.

To perform the quantum measurement tomography, we probe the decoder with input states from a set comprising all 30 elements of the six MUBs of our Hilbert space. For each measurement we make three acquisitions, each with an integration time of 10 s and an average count rate of 470 Hz. We then calculate the experimental output probabilities for each channel $p^{\gamma\xi}$, and we use them to reconstruct the POVM elements π^γ through a weighted least-squares fit:

$$\min_{\pi^\gamma} \sum_\xi \frac{\left| p^{\gamma\xi} - \text{Tr}(\rho^\xi \pi^\gamma) \right|^2}{p^{\gamma\xi}}, \tag{3}$$

where we constrain π^γ to be Hermitian and positive semidefinite. The first eigenmodes of the reconstructed POVM elements are presented in Fig. 5. One can see that they very closely match the ideal POVMs both in amplitude and in phase.

We quantify the quality of the decoder by calculating the purities of the POVM elements

$$\mathcal{P}^\gamma = \frac{\mathrm{Tr}(\pi^{\gamma 2})}{(\mathrm{Tr}\pi^\gamma)^2} \qquad (4)$$

and the fidelities when compared with the ideal operators

$$\mathcal{F}^\gamma = \sqrt{\frac{\langle\gamma|\pi^\gamma|\gamma\rangle}{\mathrm{Tr}\pi^\gamma}}. \qquad (5)$$

In an ideal system, both these values are equal to 1. The average experimental results with their respective standard deviations are listed in Table I (left column). The high average fidelity and purity indicate the remarkably good quality of the MQPG measurements.

TABLE I. Average fidelities and purities of the reconstructed POVM elements for $d = 5$ with the corresponding standard deviation.

	CCD spectrograph	TOF spectrograph
Fidelity	0.956 ± 0.014	0.810 ± 0.046
Purity	0.885 ± 0.036	0.552 ± 0.087

V. HDQKD DECODER DEMONSTRATION

To demonstrate a proof-of-principle HDQKD decoder, we need to perform photon counting. For this reason, we replace the CCD spectrograph with a homebuilt time-of-flight (TOF) fiber-assisted single-photon spectrograph [41,42]. This system exploits the chromatic group velocity dispersion of a single-mode fiber to apply various delays to the different frequency components of the pulses, effectively mapping each frequency component to a different arrival time. The arrival times are then measured with
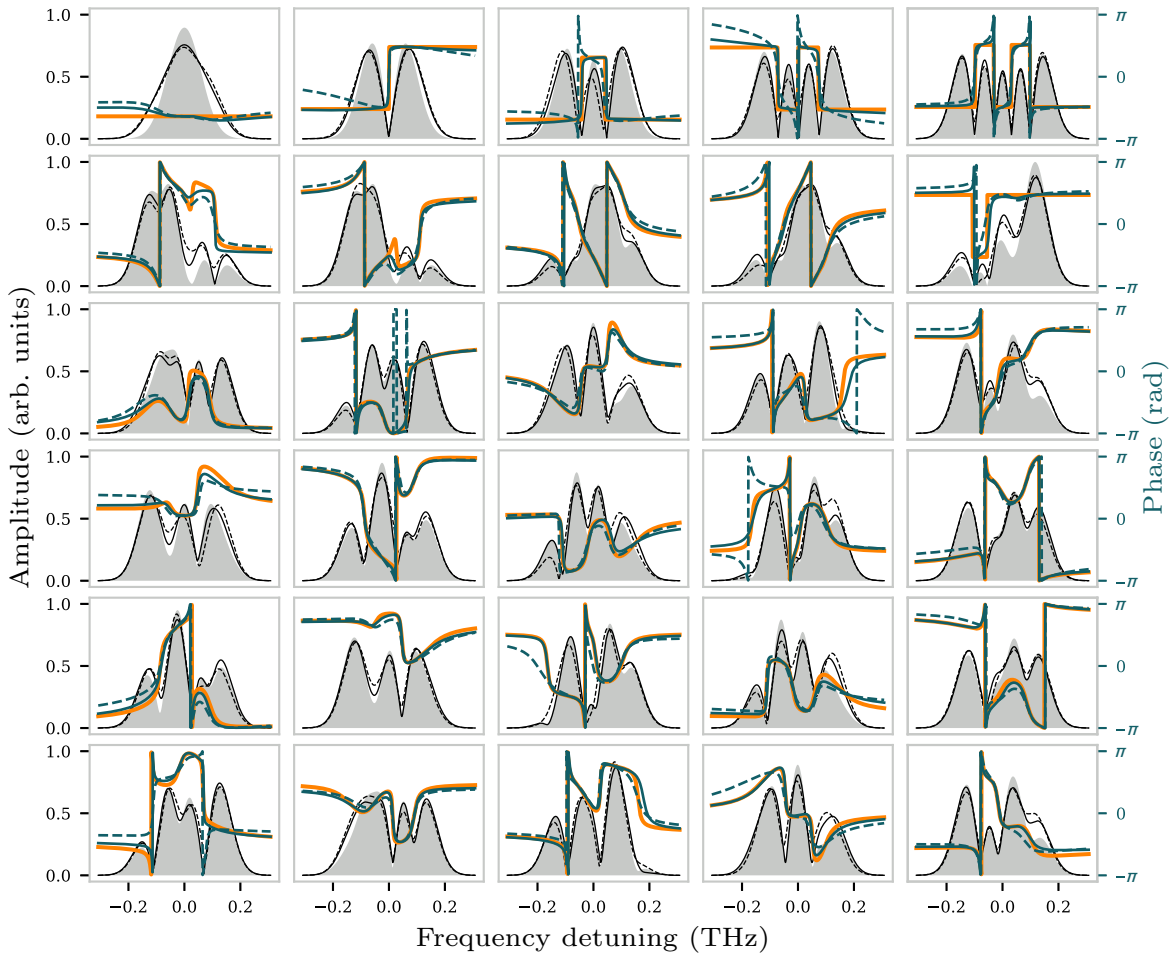

FIG. 5. First eigenmodes of the POVM elements (five for each of the six MUBs). Shaded areas and orange lines show the ideal amplitude and phase; black and blue lines show the same values for experimental data, with solid and dashed lines corresponding to the CCD spectrograph and the TOF spectrograph, respectively.

use of an avalanche photodiode combined with a time-to-digital converter. A calibration of the system then allows one to calculate the frequency corresponding to each arrival time, recovering the information on the detected TM. The simple structure of the TOF spectrograph makes it cost-effective and versatile. The TOF setup used in this experiment has a resolution of 0.3 THz and introduces 20 dB of losses. These values are limited by the availability of low-loss high-group-velocity-dispersion fibers for visible light. The high losses do not pose a fundamental problem for the operation of our decoder; however, they limit the maximum distance at which communication is still possible.

As a first characterization of the complete HDQKD decoder, we perform measurement tomography. For each measurement we make 30 acquisitions, each with an integration time of 10 s and an average count rate of 40 Hz. The characterization results, reported in Table I, show a good average fidelity. The good fidelity is apparent in the agreement between the first eigenmodes of the reconstructed POVMs and the ideal ones (Fig. 5), which show a similarly good quality for all six MUBs. The low average purity of the reconstructed POVMs, however, is an indicator of multimodedness in the decoder, which results in output clicks corresponding to TMs that are not present in the input state. The discrepancy with the high intrinsic purity of the MQPG indicates that the loss of quality can be traced back uniquely to the difference between the TOF spectrograph and the CCD spectrograph. The limited resolution of the TOF spectrograph is not sufficient to completely filter out the phase-matching imperfections of the MQPG [visible in Fig. 3(a)], which then introduce a multimode behavior in the system.

Despite the loss of quality due to the spectrograph, the decoder shows good TM-demultiplexing behavior, which makes it suitable as a proof-of-principle receiver for HDQKD. To demonstrate this, we extract the count rates relative to the projection of each input state onto the corresponding MUB from the same set of experimental data used for the tomography. We then calculate the average selectivity per MUB as the ratio of the number of correct counts to the total number of counts. Our results show an average selectivity per basis ranging from 61% to 78%, which demonstrates a clear mode-selective behavior, but indicates that there is room for improvement. Values in this range are lower than the internal average selectivity of the MQPG $\mathcal{S} = 92\%$ (measured with the CCD spectrograph). The discrepancy is once again explained by the low resolution of the TOF spectrograph used in this experiment, which hinders proper discrimination of the counts. This becomes evident when one compares the relative counts measured by the decoder in one of the six MUBs with the intrinsic performance of the MQPG (Fig. 6). This observation suggests that although the current implementation of the MQPG-based decoder is already up to the task of TM
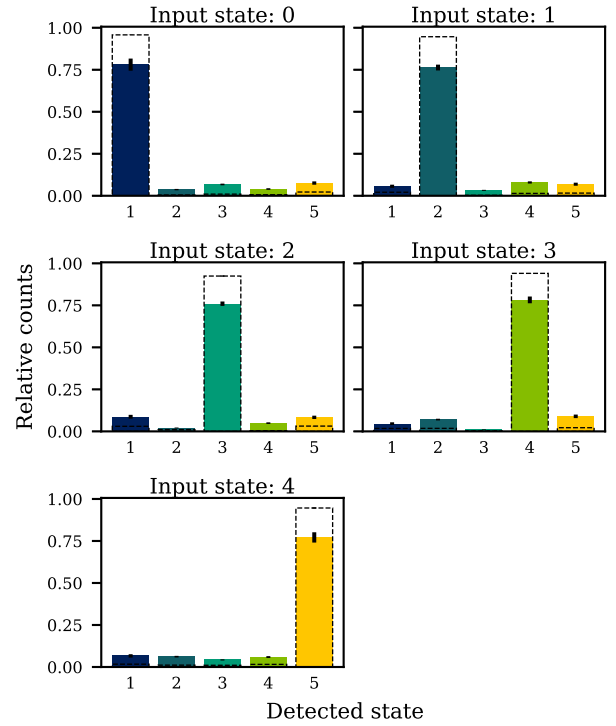

FIG. 6. Relative counts obtained when we project the five elements of one MUB onto the same MUB with the complete decoder (filled bars) and internal performance of the MQPG (dashed lines). The error bars represent the error on the mean relative counts of 30 data acquisitions.

demultiplexing, a high-resolution single-photon-resolving spectrograph will allow one to take full advantage of the high measurement quality provided by the MQPG.

VI. BEYOND QKD: STATE TOMOGRAPHY

In this section, we demonstrate that the measurement tomography of the MQPG allows us to overcome its shortcomings for applications that require measurements that become integrated over time, such as in state tomography. For this purpose, we perform resource-efficient single-photon state tomography with the MQPG and we show the improvement provided by the reconstruction of the experimental POVMs. We prepare 25 random pure input states ρ from our five-dimensional Hilbert space, and measure them using the six MUBs as decoder bases. We perform the frequency-resolved detection with the CCD camera, with three acquisitions for each measurement, each with an integration time of 10 s and an average count rate of 470 Hz. We reconstruct the input states through a weighted least-squares fit:

$$\min_{\rho} \sum_{\xi} |p^{\gamma} - \mathrm{Tr}(\rho \pi^{\gamma})|^2 / p^{\gamma}, \qquad (6)$$
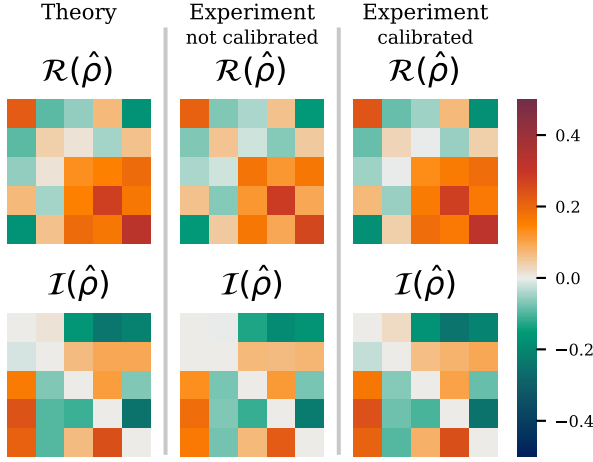
FIG. 7. Example of tomography of a random input state (measured with the CCD spectrograph). The plots correspond to the real (top) and imaginary (bottom) parts of the density matrix of, from left to right, the original input state, the raw reconstructed state, and the state reconstructed with the calibration information obtained from the measurement tomography.

where the p^γ are the output probabilities of the different channels and ρ is constrained to be Hermitian and positive semidefinite. We stress that, owing to the high dimensionality of our decoder, it is sufficient to set the pump states to the desired basis to project the input state onto all its elements at the same time within a single measurement. This means that we perform only six measurements to obtain counts on all 30 possible pump states. We highlight that the high number of measurements required constituted the main limitation to dimension scalability for the QPG [38] and that the MQPG overcomes this limitation.

We reconstruct the input state first assuming ideal POVMs $\{|\gamma\rangle\langle\gamma|\}$ ("raw" state tomography), and then considering the measured POVMs $\{\pi^\gamma\}$ ("calibrated" state tomography). The results are summarized in Table II, and an example of input-state reconstruction is provided in Fig. 7. The calibrated state tomography significantly increases the fidelity and purity of the reconstructed states. This can be explained considering that the main source of error in our system is the residual crosstalk deriving from the phase-matching imperfections, which cannot be completely eliminated even with the high resolution of the CCD spectrograph. This crosstalk is well characterized through the measurement tomography; therefore, in the calibrated state tomography we exploit this information to correct for the induced errors.

VII. DISCUSSION

The current implementation of the proof-of-principle decoder for HDQKD is limited by available components; however, the issues are of a technical nature and can be

TABLE II. Average fidelities and purities of the reconstructed input states for $d = 5$ with the corresponding standard deviation.

	Raw	Calibrated
Fidelity	0.941 ± 0.019	0.983 ± 0.016
Purity	0.816 ± 0.062	0.941 ± 0.056

overcome rather easily. The main limitation is set by the spectrograph system, which is required to be compatible with photon counting at visible wavelengths. Such a device is not yet commercially available, and the home-built TOF spectrograph used in this work introduced 20 dB of losses and had a limited resolution of 0.3 THz, which decreased the fidelity from the intrinsic value of the MQPG $\mathcal{F} = 0.96 \pm 0.01$ to the resulting decoder fidelity $\mathcal{F}' = 0.81 \pm 0.05$. The loss of fidelity can be prevented with use of state-of-the-art components for the spectrograph system. Indeed, a TOF spectrograph based on a state-of-the-art chirped fiber Bragg grating [43] and a low-jitter superconducting-nanowire single-photon detector [44] would achieve a resolution of 6 GHz for much lower losses, allowing one to fully exploit the high intrinsic fidelity of the MQPG and at the same time increase the efficiency of the decoder.

Moreover, the decoding efficiency can be further increased by increasing the internal conversion efficiency of the MQPG waveguide. This can be done through an optimized tailoring of the phase-matching function [34, 45,46] and by increasing the pump pulse energy available in the experiment. To achieve a higher pump energy, one can, of course, resort to using a higher-power laser. However, an appealing solution, with the advantage of on-chip integration, would be to generate each pump peak with a separate chip-based mode-locked laser. Indeed, preliminary devices demonstrated a spectral bandwidth of approximately 0.35 THz [47], which matches the ideal bandwidth of each pump peak of the MQPG.

Although the implemented five-channel MQPG has undeniable benefits for QC applications based on single-photon TMs (which until now have been limited to a mere two-dimensional space) one may wish to push the device to even higher dimensions. The methods detailed in Appendix A provide the scheme for generating a MQPG waveguide with the desired number of output channels via straightforward modulation of the poling pattern. The cost of moving to higher dimensions is that each pump peak becomes narrower for a fixed spectral width set by the Ti:sapphire pump pulse. To prevent a loss in measurement quality, one must either increase the available spectral bandwidth or address the difficulties that arise when one is operating with narrower and more densely spaced peaks. This requires an increased spectrograph resolution to fully discriminate the output channels, an increased shaping resolution, and a narrower phase-matching function (e.g.,

through a longer waveguide [48]) to satisfy the single-modedness condition for each channel [35]. In Appendix C, we study how improved technical capabilities can allow high-fidelity operation in higher dimensions. With state-of-the-art components, a MQPG-based decoder could easily achieve operation above 90% selectivity beyond 25 dimensions in all mutually unbiased bases.

VIII. CONCLUSION

We demonstrated five-dimensional temporal-mode demultiplexing of single photons using a newly developed device, the MQPG. We characterized its performance through measurement tomography, obtaining an average fidelity of 0.96 ± 0.01 to the theoretical POVMs. We then demonstrated a complete HDQKD decoder for single photons based on the MQPG, which revealed an average fidelity of 0.81 ± 0.05, solely limited by the currently available spectrograph technology. Finally, we exploited the information obtained from the measurement tomography of the MQPG to demonstrate resource-efficient high-quality state tomography with an average fidelity of 0.98 ± 0.02.

These results show that the demonstrated architecture provides a scalable framework for high-dimensional decoding. The purity and fidelity of the device can be easily increased by limiting the phase-matching imperfections and increasing the resolution of the spectrograph. Doing this will result in a decoder with high-performance operation in more than 25 dimensions, leading to even greater information capacity and security in HDQKD.

Finally, we highlight the versatility of the MQPG, which constitutes one of its main advantages. Because of the fully programmable shaping systems, one can easily work with alternative high-dimensional TM encodings without modifying the experimental setup. This gives one the freedom to explore a wide range of parameters so as to find the optimal solution for different applications. Finally, we emphasize that, independently of the encoding alphabet chosen and of the dimensionality d of the system, the MQPG is always able to work with the full set of $d + 1$ MUBs. This makes the MQPG a valuable resource for many QC applications and, furthermore, opens up further opportunities for all TM-based technologies, from quantum spectroscopy and metrology to quantum memories and deterministic photonic quantum gates.

APPENDIX A: MULTI-OUTPUT QUANTUM PULSE GATE

Here we describe the techniques used to obtain a MQPG process for an input signal comprising multiple temporal modes centered at telecommunication wavelengths around 1545 nm (194 THz). We start by finding the optimal parameters for a QPG process, i.e., type-II SFG between two group-velocity-matched fields labeled "pump" and "signal." To achieve group-velocity matching in a nondegenerate process, we exploit the polarization dependency of the group velocity of light in a birefringent crystal. Using this, we are able to find a transverse-magnetic-polarized pump field with different wavelength but same group velocity as the transverse-electric-polarized signal field. Next, we achieve the quasi-phase-matching condition for the chosen fields by applying a periodic poling with period Λ to the waveguide. With this method, we can identify a QPG process tailored for the chosen input wavelength, in our case a telecommunication field.

To obtain the MQPG, we need to expand the QPG process to multiple output channels. We note that, due to the properties of the QPG, each output channel will correspond to one phase-matching peak. Previous work [33,34] demonstrated that multiple phase-matching peaks are attainable through a periodic modulation of the poling pattern. We therefore modify the poling structure of a QPG waveguide by applying a modulation with period Γ ("superpoling period") and an asymmetric duty cycle $\eta \in [0, 1]$, obtaining poled regions of length $l = \eta\Gamma$ alternating with unpoled regions of length $(1 - \eta)\Gamma$ [Fig. 2(a)]. We can calculate the new phase-matching function analytically to show how this modulation generates multiple output peaks.

The phase-matching function of the SFG process for a waveguide of length L can be described as a function of the birefringent phase mismatch $\Delta\beta_u = \beta_{\text{out}} - \beta_{\text{pump}} - \beta_{\text{in}}$, where β_i is the propagation constant of field i:

$$\phi_{\text{SFG}}(\Delta\beta_u) \propto \int_0^L g(z)e^{i\Delta\beta_u z}dz, \qquad (A1)$$

where z is the position on the main waveguide axis and $g(z)$ is the nonlinearity profile along the waveguide, which is fully determined by the modulation of the poling pattern. In the range of output wavelengths allowed by energy conservation of the SFG process, the phase-matching function becomes

$$\phi_{\text{SFG}} \simeq \frac{\Gamma}{L} \frac{e^{i(\Delta\beta_u L/2)}}{e^{i(\Delta\beta_u \Gamma/2)}} \frac{\sin(\Delta\beta_u L/2)}{\sin(\Delta\beta_u \Gamma/2)} \eta \, \text{sinc}\left(\frac{\Delta\beta_p l}{2}\right) e^{i(\Delta\beta_p l/2)}, \tag{A2}$$

where we defined $\Delta\beta_p = \Delta\beta_u - 2\pi/\Lambda$. This expression describes a train of sinc-shaped peaks modulated by a sinc-shaped envelope. A quick analysis reveals that the physical
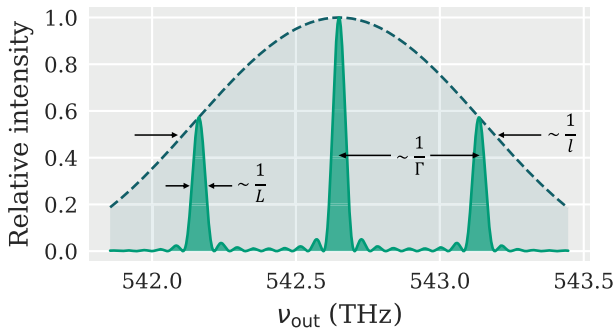
FIG. 8. Simulation of the phase-matching intensity showing how the spectral features are related to the superpoling parameters.

lengths of the waveguide are related to the spectral parameters: the length of the sample L is inversely proportional to the peak width, the superpoling period Γ is inversely proportional to the interpeak distance, and the length of each poled region l is inversely proportional to the envelope width (Fig. 8). In particular, the ratio $\Gamma/l = 1/\eta$ defines the number of peaks within the FWHM of the envelope. Therefore, the framework presented allows one to design a MQPG waveguide with the desired number of phase-matching peaks, i.e., number of output channels.

In the experimental implementation of the MQPG presented in the main text, we used a periodically poled titanium-in-diffused lithium niobate waveguide with poling period $\Lambda = 4.32$ μm operated at a working temperature of $170\,^\circ$C. The superpoling parameters were set to $l = 397$ μm and $\Gamma = 1590$ μm to obtain five output peaks in a wavelength range that would match the bandwidth of the Ti:sapphire pump $\Delta\nu_{\text{Ti:sa}} = 3$ THz used in the experiment.

APPENDIX B: REAL MQPG PROCESS

In an ideal MQPG process, each channel is characterized by single-mode operation, i.e., it provides an output only if the input signal contains the corresponding TM. This ideal behavior is exhibited only if the width of each phase-matching peak is much narrower than that of the corresponding pump pulse [35]. However, as explored in detail in previous work by our group [36], a real phase-matching function always displays some degree of imperfection [visible, for example, in Fig. 3(a)]. Phase-matching imperfections effectively broaden the width of each peak, causing multimode behavior in each channel of the MQPG process. This multimodedness then results in output clicks corresponding to TMs that are not present in the input state.

To recover single-mode operation in each channel of a real MQPG waveguide, one can exploit the fact that the frequency of the spurious output photons will be slightly offset with respect to the central output frequency of the phase-matching peak. Therefore, one can apply a spectral filter to each output channel so as to discriminate the real

counts from the spurious counts arising from the phase-matching imperfections. The method used in this work is to filter in postprocessing the output spectrum acquired by the spectrograph. We define a frequency window around the center of each output peak, and we consider as channel clicks only the counts within this window. The effectiveness of this filtering method is then dependent on the resolution of the spectrograph, which needs to be sufficiently precise to fully distinguish the phase-matching peaks from the surrounding regions.

The definition of resolution for the TOF spectrograph requires careful consideration. Since this type of spectrograph is composed of a highly dispersive fiber combined with an avalanche photodiode and a time tagger, one would intuitively define its resolution as that of the time tagger (1 ps in our case) divided by the total chromatic dispersion of the fiber (217 ps nm^{-1} for our 1 km-long fiber). However, one needs to take into account the timing jitter of the TOF setup (64 ps in FWHM), which introduces uncertainty on the arrival time of each photon, and hence on its frequency. Therefore, the actual resolution of a TOF spectrograph is given by a combination of these two factors, and in our case is dominated by the latter. This results in a much lower frequency resolution of 300 GHz, which is half as large as the separation between the peaks (630 GHz).

The effect of this low resolution is visible in Fig. 9, which shows the fidelity and the purity of the POVM elements of our decoder as a function of the window width, comparing the measurements obtained with the TOF spectrograph with those obtained with the CCD spectrograph (see Table I and Fig. 5 for reference). For the latter, which has a resolution of 30 GHz, one can notice a strong improvement of the measurement quality as the filtering window becomes narrower (from right to left), particularly in the average purity of the POVMs. This is due to the progressive elimination of spurious counts in the regions outside the phase-matching peaks. In the case of the TOF spectrograph, on the other hand, the performance improvement is barely noticeable due to its low resolution. Although it is still possible to apply a filtering window narrower than the actual resolution, we see that below 300 GHz the measurement quality is essentially saturated. The results obtained with the CCD spectrograph are therefore an indication of the high intrinsic quality of our experimental implementation of the MQPG, which could be achieved also for the decoder as a whole by solely increasing the resolution of the TOF spectrograph.

APPENDIX C: EXPANSION TO HIGHER DIMENSIONS

Here we study the maximum dimensionality achievable by a realistic MQPG-based decoder. In the system considered, the dimensionality is defined by the number of basis elements that can be observed at the same time.
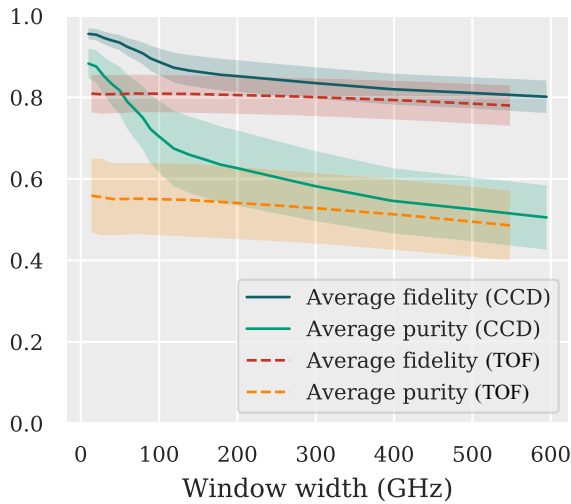
FIG. 9. Average purity and fidelity (with corresponding standard deviations) of the POVMs of our implemented five-dimensional decoder for experimental data acquired with the CCD spectrograph (solid line) and the TOF spectrograph (dashed line) as a function of the spectral window around each central frequency.
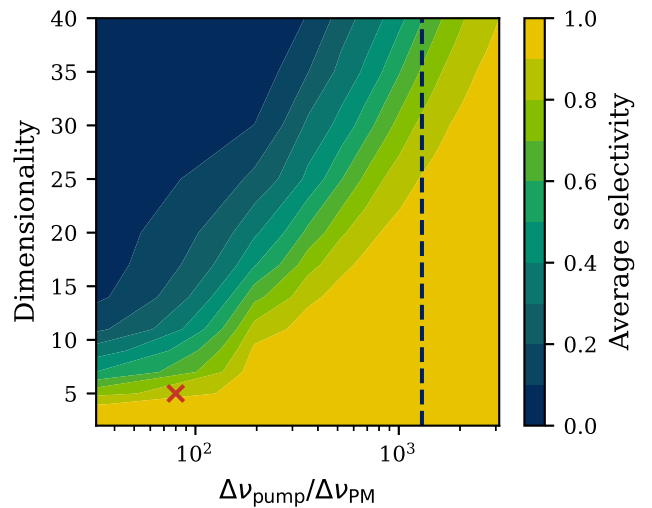

FIG. 10. Average selectivity of a MQPG-based decoder for different dimensionalities as a function of the ratio between the maximum available pump bandwidth ($\Delta\nu_{pump}$) and the bandwidth of the phase-matching function ($\Delta\nu_{PM}$). The cross marks the conditions of the experiment presented in the main text, whereas the dashed line shows what can be achieved with state-of-the-art components (a 10-cm-long sample and a pump laser bandwidth of 13 THz).

When we expand the MQPG system to the dth dimension, therefore, the Hilbert space considered will include HG modes from the zeroth order to the $(d$-1)th order and their superpositions.

We consider the case in which, as in the experimental demonstration, the pump field that drives the MQPG process is generated by shaping a single broadband pulse. The spectra corresponding to all d elements of the chosen basis ("pump peaks") must be carved within the available spectral bandwidth; therefore, the spectral width allocated for each element is inversely proportional to d. Furthermore, higher-order HG modes span a wider spectral bandwidth; as a consequence, the spectral width of each pump peak must be further reduced to avoid overlaps when one is increasing the dimensionality. This bandwidth constraint constitutes the main limitation to the scalability of the current implementation of the system. Indeed, if each pump peak is not sufficiently broader than the corresponding phase-matching peak, each channel starts displaying multimode behavior, which represents the main source of error in the experiment.

For this reason, we investigate how the ratio between the maximum available pump bandwidth and the bandwidth of the phase-matching function affects the quality of the projections, quantified as the average selectivity over all $d + 1$ MUBs of a d-dimensional Hilbert space containing HG states and their superpositions. We simulate a decoder based on a realistic MQPG waveguide in a setup with an ideal shaping resolution and an ideal noiseless spectrograph at the output of the device.

The results of the study are summarized in Fig. 10, which shows the average selectivity for all $d + 1$ MUBs of a d-dimensional MQPG-based decoder as a function of the ratio between the maximum available pump bandwidth and the bandwidth of the phase-matching function. The cross marks the conditions of the experiment presented in the main text, whereas the dashed line shows what can be achieved with state-of-the-art components: a 10-cm-long sample and a pump laser bandwidth of 13 THz would allow operation in 25 dimensions (and all 26 MUBs) with a selectivity greater than 90%.

[1] H. J. Kimble, The quantum internet, Nature **453**, 1023 (2008).

[2] J. L. O'Brien, A. Furusawa, and J. Vučković, Photonic quantum technologies, Nat. Photonics **3**, 687 (2009).

[3] J. Wang, F. Sciarrino, A. Laing, and M. G. Thompson, Integrated photonic quantum technologies, Nat. Photonics **14**, 273 (2020).

[4] L. Sheridan and V. Scarani, Security proof for quantum key distribution using qudit systems, Phys. Rev. A **82**, 030301(R) (2010).

[5] G. C. G. Berkhout, M. P. J. Lavery, J. Courtial, M. W. Beijersbergen, and M. J. Padgett, Efficient Sorting of Orbital Angular Momentum States of Light, Phys. Rev. Lett. **105**, 153601 (2010).

[6] K. Huang, H. Liu, S. Restuccia, M. Q. Mehmood, S.-T. Mei, D. Giovannini, A. Danner, M. J. Padgett, J.-H. Teng, and

C.-W. Qiu, Spiniform phase-encoded metagratings entangling arbitrary rational-order orbital angular momentum, Light: Sci. Appl. **7**, 17156 (2018).

[7] M. Mirhosseini, O. S. Magaña-Loaiza, M. N. O'Sullivan, B. Rodenburg, M. Malik, M. P. J. Lavery, M. J. Padgett, D. J. Gauthier, and R. W. Boyd, High-dimensional quantum cryptography with twisted light, New J. Phys. **17**, 033033 (2015).

[8] D. Cozzolino, B. Da Lio, D. Bacco, and L. K. Oxenløwe, High-dimensional quantum communication: Benefits, progress, and future challenges, Adv. Quantum Technol. **2**, 1900038 (2019).

[9] C. Reimer, M. Kues, P. Roztocki, B. Wetzel, F. Grazioso, B. E. Little, S. T. Chu, T. Johnston, Y. Bromberg, L. Caspani, D. J. Moss, and R. Morandotti, Generation of multiphoton entangled quantum states by means of integrated frequency combs, Science **351**, 1176 (2016).

[10] M. Kues, C. Reimer, J. M. Lukens, W. J. Munro, A. M. Weiner, D. J. Moss, and R. Morandotti, Quantum optical microcombs, Nat. Photonics **13**, 170 (2019).

[11] P. C. Humphreys, B. J. Metcalf, J. B. Spring, M. Moore, X.-M. Jin, M. Barbieri, W. S. Kolthammer, and I. A. Walmsley, Linear Optical Quantum Computing in a Single Spatial Mode, Phys. Rev. Lett. **111**, 150501 (2013).

[12] H.-H. Lu, J. M. Lukens, N. A. Peters, O. D. Odele, D. E. Leaird, A. M. Weiner, and P. Lougovski, Electro-optic Frequency Beam Splitters and Tritters for High-Fidelity Photonic Quantum Information Processing, Phys. Rev. Lett. **120**, 030502 (2018).

[13] H.-H. Lu, J. M. Lukens, N. A. Peters, B. P. Williams, A. M. Weiner, and P. Lougovski, Quantum interference and correlation control of frequency-bin qubits, Optica **5**, 1455 (2018).

[14] N. T. Islam, C. C. W. Lim, C. Cahall, J. Kim, and D. J. Gauthier, Provably secure and high-rate quantum key distribution with time-bin qudits, Sci. Adv. **3**, e1701491 (2017).

[15] I. Vagniluca, B. Da Lio, D. Rusca, D. Cozzolino, Y. Ding, H. Zbinden, A. Zavatta, L. K. Oxenløwe, and D. Bacco, Efficient Time-Bin Encoding for Practical High-Dimensional Quantum Key Distribution, Phys. Rev. Appl. **14**, 014051 (2020).

[16] B. Brecht, D. V. Reddy, C. Silberhorn, and M. G. Raymer, Photon Temporal Modes: A Complete Framework for Quantum Information Science, Phys. Rev. X **5**, 041017 (2015).

[17] M. G. Raymer and I. A. Walmsley, Temporal modes in quantum optics: then and now, Phys. Scr. **95**, 064002 (2020).

[18] F. Schlawin, K. E. Dorfman, and S. Mukamel, Pump-probe spectroscopy using quantum light with two-photon coincidence detection, Phys. Rev. A **93**, 023807 (2016).

[19] V. Ansari, B. Brecht, J. Gil-Lopez, J. M. Donohue, J. Řeháček, Z. C. V. Hradil, L. L. Sánchez-Soto, and C. Silberhorn, Achieving the Ultimate Quantum Timing Resolution, PRX Quantum **2**, 010301 (2021).

[20] M. Mazelanik, A. Leszczyński, and M. Parniak, Optical-domain spectral super-resolution via a quantum-memory-based time-frequency processor, Nat. Commun. **13**, 691 (2022).

[21] J. Nunn, I. A. Walmsley, M. G. Raymer, K. Surmacz, F. C. Waldermann, Z. Wang, and D. Jaksch, Mapping broadband single-photon wave packets into an atomic memory, Phys. Rev. A **75**, 011401(R) (2007).

[22] M. Afzelius, C. Simon, H. de Riedmatten, and N. Gisin, Multimode quantum memory based on atomic frequency combs, Phys. Rev. A **79**, 052329 (2009).

[23] Z. Zheng, O. Mishina, N. Treps, and C. Fabre, Atomic quantum memory for multimode frequency combs, Phys. Rev. A **91**, 031802(R) (2015).

[24] G. Harder, V. Ansari, B. Brecht, T. Dirmeier, C. Marquardt, and C. Silberhorn, An optimized photon pair source for quantum circuits, Opt. Express **21**, 13975 (2013).

[25] T. C. Ralph, I. Söllner, S. Mahmoodian, A. G. White, and P. Lodahl, Photon Sorting, Efficient Bell Measurements, and a Deterministic Controlled-Z Gate Using a Passive Two-Level Nonlinearity, Phys. Rev. Lett. **114**, 173603 (2015).

[26] S. Gao, O. Lazo-Arjona, B. Brecht, K. T. Kaczmarek, S. E. Thomas, J. Nunn, P. M. Ledingham, D. J. Saunders, and I. A. Walmsley, Optimal Coherent Filtering for Single Noisy Photons, Phys. Rev. Lett. **123**, 213604 (2019).

[27] V. Ansari, E. Roccia, M. Santandrea, M. Doostdar, C. Eigner, L. Padberg, I. Gianani, M. Sbroscia, J. M. Donohue, and L. Mancino, *et al.*, Heralded generation of high-purity ultrashort single photons in programmable temporal shapes, Opt. Express **26**, 2764 (2018).

[28] X. Shi, A. Valencia, M. Hendrych, and J. P. Torres, Generation of indistinguishable and pure heralded single photons with tunable bandwidth, Opt. Lett. **33**, 875 (2008).

[29] P. J. Mosley, J. S. Lundeen, B. J. Smith, P. Wasylczyk, A. B. U'Ren, C. Silberhorn, and I. A. Walmsley, Heralded Generation of Ultrafast Single Photons in Pure Quantum States, Phys. Rev. Lett. **100**, 133601 (2008).

[30] B. Brecht, A. Eckstein, R. Ricken, V. Quiring, H. Suche, L. Sansoni, and C. Silberhorn, Demonstration of coherent time-frequency Schmidt mode selection using dispersion-engineered frequency conversion, Phys. Rev. A **90**, 030302(R) (2014).

[31] V. Ansari, J. M. Donohue, M. Allgaier, L. Sansoni, B. Brecht, J. Roslund, N. Treps, G. Harder, and C. Silberhorn, Tomography and Purification of the Temporal-Mode Structure of Quantum Light, Phys. Rev. Lett. **120**, 213601 (2018).

[32] D. V. Reddy and M. G. Raymer, High-selectivity quantum pulse gating of photonic temporal modes using all-optical Ramsey interferometry, Optica **5**, 423 (2018).

[33] M. Silver, Y. Huang, C. Langrock, M. Fejer, P. Kumar, and G. Kanter, Three-signal temporal-mode selective upconversion demultiplexing, IEEE Photonics Technol. Lett. **31**, 1749 (2019).

[34] M. H. Chou, K. R. Parameswaran, M. M. Fejer, and I. Brener, Multiple-channel wavelength conversion by use of engineered quasi-phase-matching structures in LiNbO$_3$ waveguides, Opt. Lett. **24**, 1157 (1999).

[35] J. M. Donohue, V. Ansari, J. Řeháček, Z. Hradil, B. Stoklasa, M. Paúr, L. L. Sánchez-Soto, and C. Silberhorn, Quantum-Limited Time-Frequency Estimation through Mode-Selective Photon Measurement, Phys. Rev. Lett. **121**, 090501 (2018).

[36] M. Santandrea, M. Stefszky, V. Ansari, and C. Silberhorn, Fabrication limits of waveguides in nonlinear crystals and their impact on quantum optics applications, New J. Phys. **21**, 033038 (2019).

[37] J. S. Lundeen, A. Feito, H. Coldenstrodt-Ronge, K. L. Pregnell, C. Silberhorn, T. C. Ralph, J. Eisert, M. B. Plenio, and I. A. Walmsley, Tomography of quantum detectors, Nat. Phys. **5**, 27 (2009).

[38] V. Ansari, G. Harder, M. Allgaier, B. Brecht, and C. Silberhorn, Temporal-mode measurement tomography of a quantum pulse gate, Phys. Rev. A **96**, 063817 (2017).

[39] A. Monmayrant, S. Weber, and B. Chatel, A newcomer's guide to ultrashort pulse shaping and characterization, J. Phys. B—At., Mol. Opt. Phys. **43**, 00 (2010).

[40] C. K. Law, I. A. Walmsley, and J. H. Eberly, Continuous Frequency Entanglement: Effective Finite Hilbert Space and Entropy Control, Phys. Rev. Lett. **84**, 5304 (2000).

[41] M. Avenhaus, A. Eckstein, P. J. Mosley, and C. Silberhorn, Fiber-assisted single-photon spectrograph, Opt. Lett. **34**, 2873 (2009).

[42] F. Marsili, V. B. Verma, J. A. Stern, S. Harrington, A. E. Lita, T. Gerrits, I. Vayshenker, B. Baek, M. D. Shaw, R. P. Mirin, and S. W. Nam, Detecting single infrared photons with 93% system efficiency, Nat. Photonics **7**, 210 (2013).

[43] A. O. C. Davis, P. M. Saulnier, M. Karpiński, and B. J. Smith, Pulsed single-photon spectrometer by frequency-to-time mapping using chirped fiber Bragg gratings, Opt. Express **25**, 12804 (2017).

[44] B. Korzh, *et al.*, Demonstration of sub-3 ps temporal resolution with a superconducting nanowire single-photon detector, Nat. Photonics **14**, 250 (2020).

[45] A. M. Brańczyk, A. Fedrizzi, T. M. Stace, T. C. Ralph, and A. G. White, Engineered optical nonlinearity for quantum light sources, Opt. Express **19**, 55 (2011).

[46] D. Zhu, L. Shao, M. Yu, R. Cheng, B. Desiatov, C. J. Xin, Y. Hu, J. Holzgrafe, S. Ghosh, A. Shams-Ansari, E. Puma, N. Sinclair, C. Reimer, M. Zhang, and M. Lončar, Integrated photonics on thin-film lithium niobate, Adv. Opt. Photonics **13**, 242 (2021).

[47] C. Gordón, R. Guzmán, V. Corral, X. Leijtens, and G. Carpintero, On-chip colliding pulse mode-locked laser diode (OCCP-MLLD) using multimode interference reflectors, Opt. Express **23**, 14666 (2015).

[48] J. Gil-Lopez, M. Santandrea, G. Roland, B. Brecht, C. Eigner, R. Ricken, V. Quiring, and C. Silberhorn, Improved non-linear devices for quantum applications, New J. Phys. **23**, 063082 (2021).